

# Mesoscale eddy variability in the Caribbean Sea.\*

Margarita E. López-Álzate<sup>1,2</sup>, Juan-Manuel Sayol<sup>3</sup>, Ismael Hernández-Carrasco<sup>4</sup>, Andrés F. Osorio<sup>1,2</sup>, Evan Mason<sup>5</sup> and Alejandro Orfila<sup>5\*</sup>

<sup>1</sup>Oceánicos, Facultad de Minas. Universidad Nacional de Colombia. Medellín, Colombia.

<sup>2</sup>CEMarin. Carrera 21 # 35-53, Barrio La Soledad, Bogotá, Colombia.

<sup>3</sup>Department of Applied Mathematics. , University of Alicante, San Vicente del Raspeig, 03690, Alicante, Spain.

<sup>4</sup>Balearic Islands Coastal Observing and Forecasting System (SOCIB), Palma, 07122, Mallorca, Spain.

<sup>5\*</sup>Mediterranean Institute for Advanced Studies, IMEDEA (CSIC-UIB), Esporles, 07190, Mallorca, Spain.

\*Corresponding author(s). E-mail(s): [alejandro.orfila@csic.es](mailto:alejandro.orfila@csic.es);  
 Contributing authors: [melojeza@unal.edu.co](mailto:melojeza@unal.edu.co) ;  
[juanma.sayol@ua.es](mailto:juanma.sayol@ua.es); [ihernandez@socib.es](mailto:ihernandez@socib.es) ;  
[afosorioar@unal.edu.co](mailto:afosorioar@unal.edu.co) ; [evanmason@gmail.com](mailto:evanmason@gmail.com);

## Abstract

The spatial distribution, the monthly and seasonal variability of mesoscale eddy-observations derived from the AVISO eddy atlas are assessed in the Caribbean Sea for the period between 1993 and 2019 (both included). The average lifetime for the whole set of eddies is  $61.8 \pm 37.1$  days, mean amplitude of  $7.4 \pm 4.2$  cm for cyclonic and  $6.7 \pm 3.7$  cm for anticyclonic and mean radius of  $99.5 \pm 31.2$  km for cyclonic and  $108.0 \pm 32.4$  km for anticyclonic. Cyclonic eddies are on average more

---

\*This work will be submitted to Ocean Dynamics. Copyright in this work may be transferred without further notice. The paper is a non-peer reviewed preprint submitted to EarthArXiv

047 non-linear than anticyclonic. The spatio-temporal variability in the num-  
048 ber of eddy-observations is evaluated against the Mean Eddy Kinetic  
049 Energy (MEKE) derived from geostrophic currents as well as from sea-  
050 sonal winds. Spatial distribution of eddy-observations are correlated  
051 with MEKE while the migration of the intertropical convergence zone  
052 explains the advection of eddies towards the southern part of the basin.

053 **Keywords:** Mesoscale eddies, Caribbean Sea, seasonal variability,  
054 self-organizing map (SOM), eddy-observations

## 055 056 057 058 **1 Introduction** 059

060 Mesoscale eddies are ocean structures in nearly geostrophic balance of  
061 paramount importance in the redistribution of water properties across ocean  
062 basins (Capet et al, 2008; Farneti et al, 2010; Gaube et al, 2015). These vortexes  
063 have diameters that oscillate between 5 and 200 km and lifetimes spanning  
064 from weeks to months (Chelton et al, 2011).

065 Mesoscale eddies typically form from initial instabilities created by the  
066 interaction between strong horizontally sheared currents or from current-  
067 topography interactions in boundary currents (Bracco et al, 2008; Rennie et al,  
068 2007; Soutelino et al, 2013), although other mechanisms may exist (e.g., Ji  
069 et al, 2018). Depending on which side with respect to the main flow they form,  
070 eddies may contain either relatively warm or cold water compared to their sur-  
071 roundings. Accordingly, eddies will rotate anticyclonically or cyclonically in the  
072 Northern Hemisphere. Warm-core eddies display a central Sea Surface Height  
073 (SSH) of a few to tens of centimeters higher than outer water, while cold-core  
074 eddies present a central SSH lower than its surroundings. Despite warm-core  
075 eddies can trap and transport a wide variety of nutrients and aquatic life  
076 (Karstensen et al, 2017), cold-core eddies tend to carry a greater amount  
077 of biological activity with them (Chang et al, 2018). Sometimes, mesoscale  
078 eddies may also take the form of well defined rings that extend to large depths  
079 (Fratantoni and Richardson, 2006; de Jong et al, 2016).

080 Previous experimental and numerical studies have suggested that mesoscale  
081 variability in the Caribbean Sea is dominated by warm-core anticyclonic  
082 eddies. Regarding their mechanisms of formation, some authors have associ-  
083 ated the formation of Caribbean Sea eddies with flow-topography interaction  
084 (Jouanno et al, 2008, 2009; van der Boog et al, 2019; Molinari et al, 1981; Goni  
085 and Johns, 2003; Jochumsen et al, 2010), the meandering of the Caribbean  
086 boundary current (Andrade and Barton, 2000), and the growth of baro-  
087 clinic instabilities around river plume fronts (Chérubin and Richardson, 2007).  
088 Indeed some eddies form from cold filaments at the eastern side of the basin  
089 thus leading to a cooling of the Caribbean Sea interior, whilst at the same  
090 time they transport salinity anomalies from Amazon and Orinoco river plumes  
091 westward (van der Boog et al, 2019).

In the Caribbean, eddies are transported westward by the mean flow after their formation, thus entirely affecting the ecosystem around them as they transport larvae and nutrients offshore (Andrade and Barton, 2005; Baums et al, 2006). During their propagation, eddies become more energetic and increase their amplitude (Carton and Chao, 1999; van der Boog et al, 2019). Although this intensification is evident from observations, only a few studies have elaborated the dynamics of this strengthening (Carton and Chao, 1999; Pauluhn and Chao, 1999; Andrade and Barton, 2000; Richardson, 2005). Based on surface drifters, Richardson (2005) suggested that the anticyclonic shear of the Caribbean Current could amplify anticyclonic eddies. Besides, Andrade and Barton (2000) found, based on satellite altimetry, a direct relationship between the maximum curl of the wind stress and the westward intensification of anticyclones. Jouanno et al (2009) used a regional model to study the life cycle of Caribbean anticyclones and computed the mechanical energy balance of the flow in this region. Although this balance shows that baroclinic instabilities provide the necessary energy for the westward growth of anticyclones, it does not explain what drives the westward intensification of anticyclones. More recently, van der Boog et al (2019) have mainly attributed this westward intensification of anticyclonic eddies to the role of salinity gradients generated by upwelling events and river outflow combined with the westward rise of the background velocity shear, which altogether strengthen the thermal wind balance within the vortex.

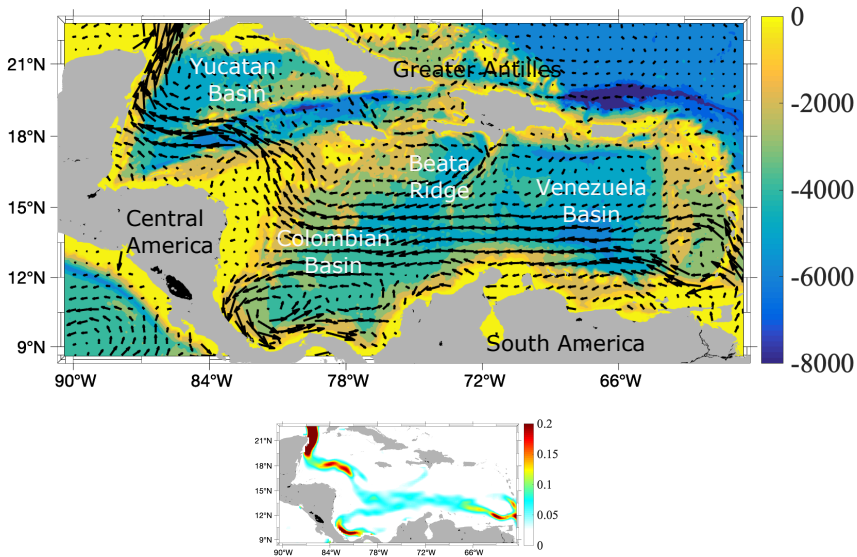
From the above background, in this work we analyze the spatial and temporal variability of observed mesoscale eddies from 1993 to 2019 (both included). To our knowledge, neither a dedicated systematic census of observed eddies focused on the Caribbean Sea nor an analysis of their seasonal variability from a statistical standpoint have been performed yet, beyond some global studies (e.g., Chelton et al, 2011; Mason et al, 2014; Conti et al, 2016). In this work, we address this gap by providing a detailed statistical description of eddy-properties, as well as of the main environmental drivers that may affect their seasonal variability.

## 2 The Caribbean basin

The Caribbean is a semi-enclosed sea that covers the area between 8°N – 25°N and 85°W – 55°W (Fig. 1). It is confined on the south and west by the South and Central American continents, and on the north and the east by the Greater Antilles and the chain of Lesser Antilles Islands Arc (Andrade, 2000; Johns et al, 2002; Richardson, 2005; Jury, 2011). The Caribbean Sea is connected by many passages to the tropical Atlantic Ocean through the Lesser Antilles (Fig. 1, a). According to its bottom topography, the Caribbean Sea can be divided into five basins: between the Lesser Antilles Arc and Las Aves Ridge lies the Granada Basin, the Venezuelan Basin in the east, and the Colombian Basin in the west. These basins are separated by the Beata Ridge which crosses the central Caribbean. The Central American Rise separates

4 *Mesoscale eddy variability in the Caribbean Sea*

139 the Cayman and Colombian Basins and the Cayman Ridge which divides the  
 140 Cayman and Yucatan Basins. The Caribbean Sea is connected with the Gulf  
 141 of Mexico at the north through the Yucatan Strait.



163 **Fig. 1** Top: Geographic location of the Caribbean Sea with the different basins and  
 164 bathymetry contour (in m). Arrows correspond to the mean geostrophic currents for the  
 165 period 1993–2019 derived from AVISO SLA. Bottom: MKE ( $u_g^2 + v_g^2$ ) obtained from  
 166 geostrophic velocities for the period 1993–2019 (units in  $m^2/s^2$ ). We use the geostrophic  
 167 velocities derived from two-satellite delayed sea level time series. This data is available since  
 168 1993 at Copernicus Climate Change Service (<https://climate.copernicus.eu/>), with spatial  
 169 resolution of  $0.25^\circ \times 0.25^\circ$  (only each 9 arrows have been plotted for simplicity).

171 The most important sources of water in the Caribbean Sea are provided  
 172 by the returning deep southwestward Gulf Stream waters in the northern and  
 173 northeastern edges, and by the North Brazil Current (NBC) on the southeast-  
 174 ern edge (Fig. 1, a). Atlantic waters contribute in three different ways: the  
 175 North Equatorial Current passing through the Leeward Islands of the Lesser  
 176 Antilles with an estimated inflow of  $\sim 8$  Sv, the flow in the windward Passage  
 177 between Cuba and Hispaniola with  $\sim 7$  Sv, and the flow through the Mona  
 178 Passage between Hispaniola and Puerto Rico with  $\sim 3$  Sv. The NBC bears  
 179 fresh water from the Orinoco River, flowing northwestward into the Caribbean  
 180 basin through the “Windward Island” with  $\sim 6$  Sv and Saint Vincent and Saint  
 181 Lucia with  $\sim 4$  Sv forming a boundary current known as the Caribbean Current  
 182 (CC) (Richardson, 2005; Jury, 2011). The CC extends towards the Panama  
 183 Isthmus where a branch continues towards the Yucatan basin, while another  
 184 branch may recirculate to form the Panama-Colombia Gyre, from which under

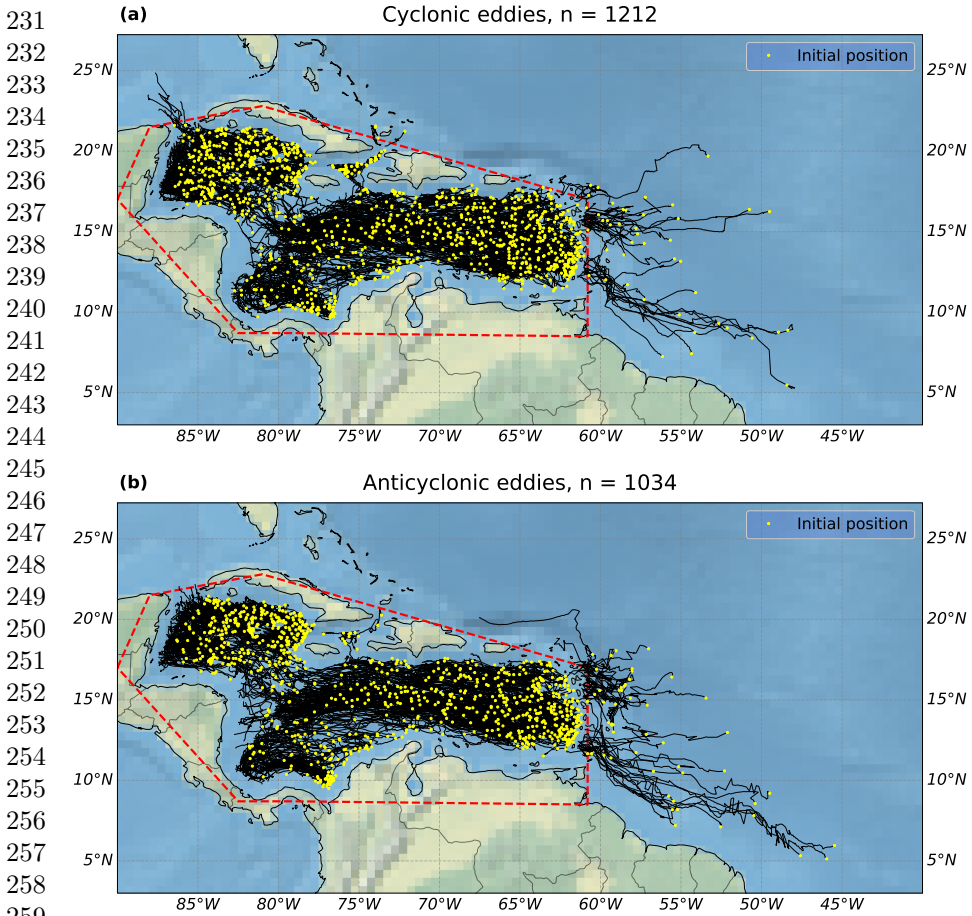
favorable wind conditions a counter current can form and reach La Guajira peninsula, known as the Caribbean Counter Current (CCC) (Orfla et al, 2021).

A strong Ekman component of the transport is generated in the Caribbean Sea by the Trade Winds (see Fig. A1 in the Appendix A), which blow from the northeast-east-southeast depending, to a large extent, on the latitudinal position of the Intertropical Convergence Zone (ITCZ) and of the North Atlantic subtropical high Schneider et al (2014); Orejarena-Rondón et al (2022).

### 3 Eddy trajectory atlas

Detected eddies for the period between 1993 and 2019 are obtained from the eddy trajectory atlas in its delayed-time version 2.0exp. This product provides information on mesoscale eddies derived from Sea Level Anomalies (SLA) and it is produced by SSALTO/DUACS and distributed by AVISO+ with support from CNES, Oregon State University and NASA (AVISO, 2020). The atlas includes information on weekly properties of each detected eddy such as radius, amplitude, rotational speed, polarity as well as the time when it was observed, the coordinates of the estimated center, the track identification or the observation number. The algorithms used in this product are derived from the methodology developed by Schlax and Chelton (2016), where an eddy is considered to be a propagating, compact, coherent structure in the space-time SSH field. Among the processes followed by the algorithm are included the filtering of sea level anomalies, the eddy-identification, the characterization of main properties of eddies (size, amplitude, rotational speed) and the eddy tracking. Throughout next sections and for the sake of clarity we will refer by eddy-observation every single daily data of a given track, while by an eddy we will refer to the statistical average of all available observations for the same track. For further details on the eddy detection algorithm the reader is referred to the Appendix B.

The number of detected eddies during 1993–2019 in the Caribbean basin (red box in Fig. 2) is 2246 (only 110 detected outside, between 5 and 15° N) almost equally distributed between cyclonic eddies (CE) (54%) and anticyclonic eddies (AE) (46%). The initial positions (yellow dots) and trajectories are displayed in Fig. 2 for CE (a) and for AE (b). As seen, most eddies have their origin in the eastern Caribbean Sea and in the northwestern side. In the former case, eddies are advected by the CC whose origin is the North Equatorial Current passing through the Lesser Antilles and deflected at 76°W towards the south of Panama following the CCC. Both the CC and the CCC are clearly recognizable from the Mean Kinetic Energy ( $\text{MKE} = u_g^2 + v_g^2$ ) of the geostrophic currents,  $\mathbf{v}_g$  (see Fig. 1, b).

6 *Mesoscale eddy variability in the Caribbean Sea*

260 **Fig. 2** Trajectories of eddies for the period between 1993 and 2019 (both included) from  
 261 the AVISO atlas: (a) for cyclonic eddies (CE) and (b) for anticyclonic eddies (AE). The  
 262 dashed red line delimits the area of study and yellow dots indicate initial location of eddies.

## 263 4 Results

### 264 4.1 Statistical description of Caribbean Sea 265 eddy-properties

266 Mean and standard deviation of observed eddies in the Caribbean Sea are  
 267 shown in Fig. 3 for relevant parameters: lifetime (a-c), amplitude (d-f), radius  
 268 (g-i) and nonlinearity (j-l).

269 The average lifetime for the whole set of eddies is  $61.8 \pm 37.1$  days (mean  
 270  $\pm$  standard deviation), and  $59.7 \pm 34.7$  days for CE and  $64.3 \pm 39.7$  days  
 271 for AE with the longest-lived lasting 319 days and 290 days for CE and AE,  
 272 respectively (Fig. 3, a-c). A vast majority of mesoscale eddies ( $> 85\%$ ) have a  
 273 lifetime shorter than 120 days.  
 274  
 275  
 276

The eddy amplitude, defined as the largest sea level gradient between the eddy core and the sea level height average at its edge perimeter is shown in Fig. 3,d-f. Mean amplitude is  $7.4 \pm 4.2$  cm for CE (Fig. 3,e) and  $6.7 \pm 3.7$  cm for AE (Fig. 3,f). These results agree with those of Gaube (2013), who found that the eddy field in the Caribbean Sea is characterized by average eddy amplitudes of 7.1 cm. However, Chelton et al (2011) pointed out that the predominance of small eddy amplitudes may raise concerns that their distribution is influenced by the procedure applied to detect eddies, which may sometimes be biased low by 1 or 2 cm in regions of very energetic mesoscale variability and by less than 1 cm in less energetic regions due to the complex geometry of many eddies.

There are no significant differences between both eddy polarities in the effective radius scale. Radii range from 50 to 250 km, as expected from the spatial resolution of the altimetry. The mean radius is  $99.5 \pm 31.2$  km for CE and  $108.0 \pm 32.4$  km for AE (Fig. 3,h-i). This result is consistent with the latitudinal distribution of eddy sizes described by Chelton et al (2011), where eddies of around 100 km of radius are found in the near-equatorial regions to later monotonically decrease up to 80 km at  $20^\circ$  of latitude. We note that these length-scales of eddies and eddy-like features are constrained by the Rossby radius of deformation (Chelton et al, 1998).

The eddy nonlinearity is defined as,  $\varepsilon = U/c$  with  $U$  being the rotational speed and  $c$  the celerity of the advection on the geostrophic flow, also called translational speed. A value of  $\varepsilon \geq 1$  implies that the mesoscale eddy cannot be regarded as a linear wave disturbance propagating through a nearly stationary medium, but instead is capable of modifying the medium by advecting a trapped fluid parcel as it translates transporting water properties such as heat and salt, as well as other biogeochemical characteristics such as nutrients and phytoplankton (Chelton et al, 2011). Fig. 3j-l shows that, all combined, CE and ACE are nonlinear on average, with over 90% of eddies showing  $\varepsilon \geq 1$ . Indeed, over 25% of eddies are highly nonlinear with  $\varepsilon > 5$ , being CE more nonlinear than ACE on average ( $4.8 \pm 4.1$  against  $3.9 \pm 3.1$ ). These values of  $\varepsilon$  are in good agreement with the results that can be inferred from Chelton et al (2011) in the Caribbean Sea region.

To examine the general patterns in the eddy properties we have proceeded to normalize the amplitude, radii and nonlinearity of eddies according to their lifetime. To this end, for each eddy the first value of lifetime is considered its birth (normalized lifetime of 0), and the last value its death (normalized lifetime of 1). Subsequently, the lifetime of each eddy has been divided in regular sub periods of 0.02. Later, the mean value of each parameter within each sub period has been computed and scaled with respect to the value at birth, which provides a normalized value of 1 for each eddy and for all properties at the initial time. Finally, all eddy-observations within the corresponding sub period have been averaged. As a result, a general mean curve showing the evolution of each eddy property for all eddy-observations and for a normalized lifetime is obtained.

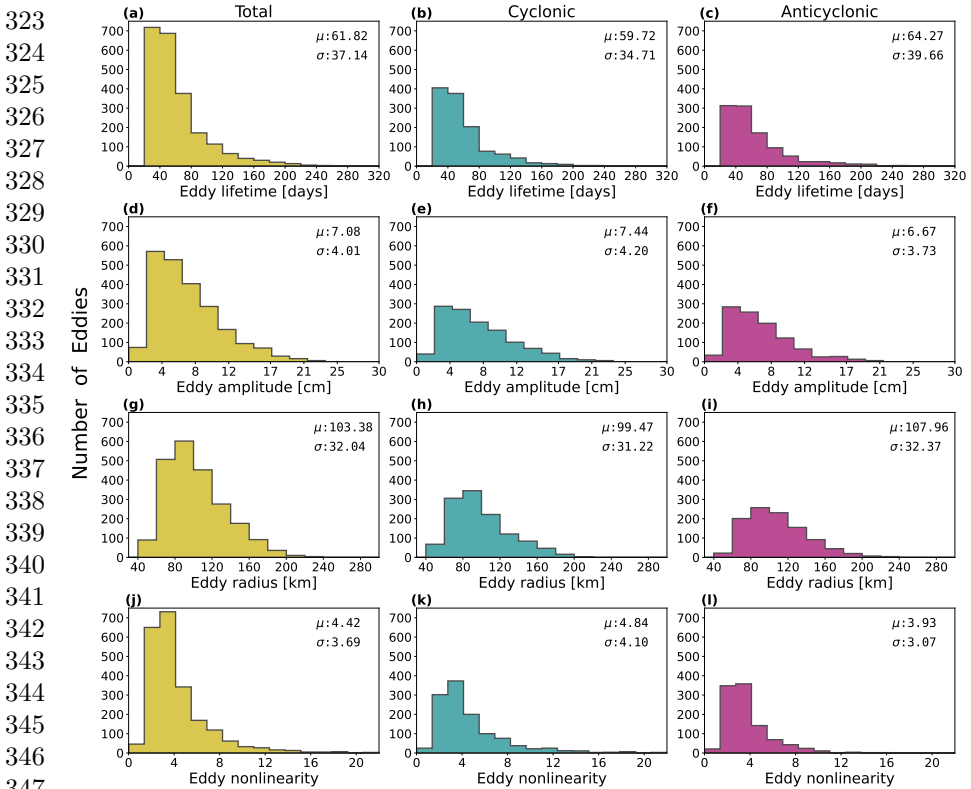


**Fig. 3** Histogram of properties for the total number of eddies (left), for CE (center) and for AE (right). First row correspond to eddy lifetime (in days), second to amplitude (in cm), third radius (in km), and fourth nonlinearity (dimensionless).

Results for the amplitude, radii and nonlinearity for the whole set of eddies, CE and AE are displayed in Fig. 4. As seen, when all eddies are considered, they tend to increase substantially in amplitude and radius during the first part of their life (around 150% in amplitude and 35% in radius) reaching the maximum development at around 0.6 of their normalized lifetime (Fig.4,a). The same trend is obtained for the CE and AE subset of data (Fig. 4, b and c, respectively). Once eddies have reached their maximum amplitude they tend to spend another 20% of their lifetime with the same amplitude, to later start a fast decay till reaching a value close to 50% larger of their initial amplitude at the end of their lifetime. A similar process occurs with the radii, with small differences between AE and CE. At the end of their life, the radius tends to be about 10% larger than in the beginning. An interesting point is that the peak in amplitude is clearer defined for CE than for ACE, since the latter shows a plateau for about 20% of normalized eddy lifetime. Hence, this result could be potentially used to predict eddy lifetime of CE, partially disagreeing with the statement of [Chelton et al \(2011\)](#), who argued that the amplitude of an eddy is not enough to determine its longevity. Regarding non-linearity, it strongly



increases (about 200%) on average during the first third of eddy lifetime, then it keeps rather stable although with some marked oscillations, which suggests large differences between eddies. At the end of their observed life, eddies are about 2.5–3 times more nonlinear than in the beginning.

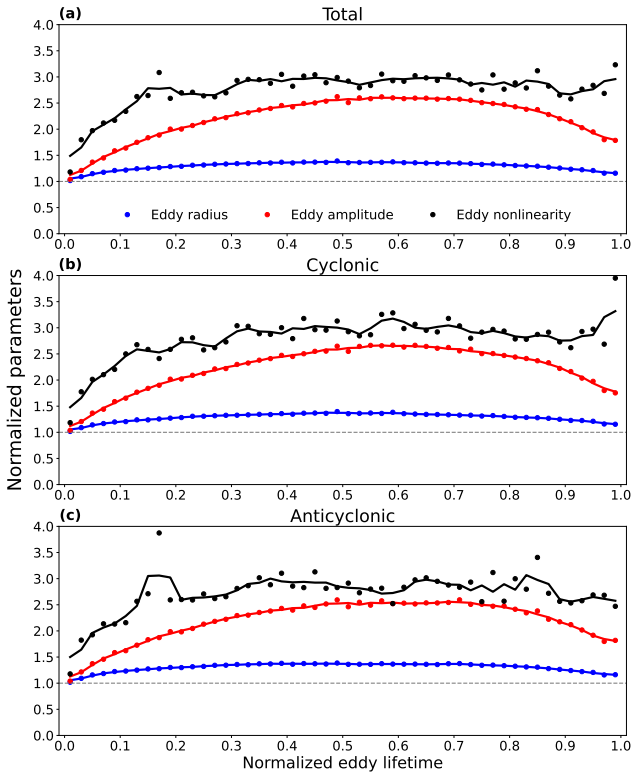


**Fig. 4** Mean properties of eddies normalized by their lifetime and scaled by their initial value. Blue line corresponds to amplitude, red line corresponds to radius, and black line for eddy nonlinearity: a) for the total # of eddies; b) for CE and c) for AE. Solid lines represent a 3-point moving average, except in the extremes (2-point average).

## 4.2 Spatial distribution of Caribbean Sea eddies

The total number of eddy-observations (summed up in squares of  $0.5 \times 0.5^\circ$ ) are displayed in Fig. 5, left panel. At the northern basin, eddies are distributed in the whole domain with a larger number of observations at the edges constrained by the 500 m isobath, and the two branches flowing northwards, towards the Yucatan channel, and southwards, forming the Caribbean counter-current (CCC) near Panama. Jouanno et al (2008), already described permanent features involved in the formation/dissipation of eddies consisting of an anticyclonic recirculation of water in the south of Cuba and a cyclonic

415 gyre, known as the Panama-Colombia gyre, characterized by the episodic for-  
 416 mation of CE that quickly dissipate when interact to the southern Caribbean  
 417 anticyclones.

418 Above features are illustrated by the Mean Eddy Kinetic Energy (MEKE),  
 419 defined as  $MEKE = u_g'^2 + v_g'^2$ , where the prime stand for the time-dependent  
 420 fluctuating part (the eddy component of the flow), averaged over 1993–2019,  
 421 which is shown in Fig. 5, right. As expected, high values of MEKE correspond  
 422 to the locations where the largest number of eddies are found (Fig. 5, left  
 423 panel). MEKE has been computed with daily geostrophic velocities over the  
 424 basin and its primary source of generation is the mean current instability,  
 425 which acts in two ways to generate eddies; first, strong horizontally sheared  
 426 motions result in barotropic instabilities where the energy source for generating  
 427 eddies is the MKE, and secondly, the presence of a vertical shear in strong  
 428 ocean fronts results in baroclinic instabilities where the energy required for  
 429 eddy generation comes from the available potential energy due to isopycnal  
 430 tilting. Both formation processes lead to hot spots of eddy energy.

431

432

433

434

435

436

437

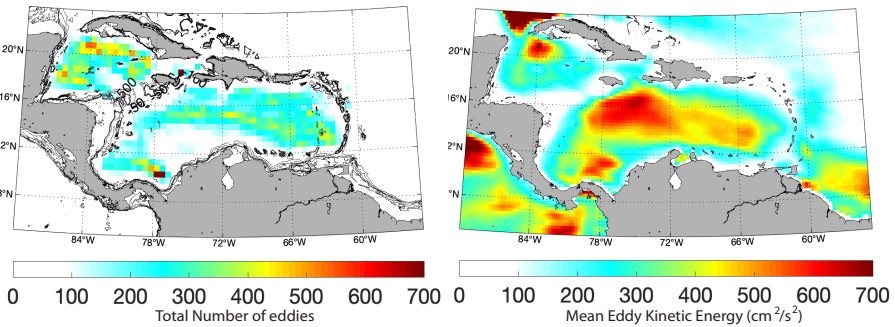
438

439

440

441

442



443 **Fig. 5** Left: Total number of eddy-observations from 1993 to 2019 within boxes of  $0.5^\circ \times 0.5^\circ$   
 444 side length. Isolines depict the 50, 100, 200, 500 and 1000 m isobaths. Right: MEKE derived  
 445 from SSH geostrophic velocities for the period of 1993 to 2019. Units in  $\text{cm}^2/\text{s}^2$ .

446

447

448

449

450

451

452

453

454

455

456

457

458

459

460

Winds in the Caribbean are mainly driven by the location of the ITCZ and  
 by the American Monsoon System, and present two climatic seasons: the dry  
 season from December to March, and the wet season from August to Novem-  
 ber. During the dry season, northern easterlies dominate the area due to the  
 location of the ITCZ at a latitude between  $0^\circ\text{N}$  and  $5^\circ\text{N}$ . During the wet season  
 southern easterlies are able to reach the Colombian basin due to the migration  
 of ITCZ towards higher latitudes (between  $10^\circ\text{N}$  and  $12^\circ\text{N}$ ) (Orejarena-Rondón  
 et al, 2019). Averaged wind streamlines for dry and wet seasons are depicted  
 in Fig. 6, left and right panels respectively (see for completeness Fig. A1 in the  
 Appendix for the monthly mean wind patterns over the Caribbean Sea). The  
 spatial distribution of eddy-observations during these two seasons (shading in  
 both panels) shows a shift in the southern area of the basins between Panama  
 and Colombia with more eddies approaching the continent. This is proba-  
 bly the result of the intensification of the Caribbean Countercurrent (CCC)

induced by the shift of the ITCZ, which advects eastwards those eddies formed by the instability of the CC in the central basin.

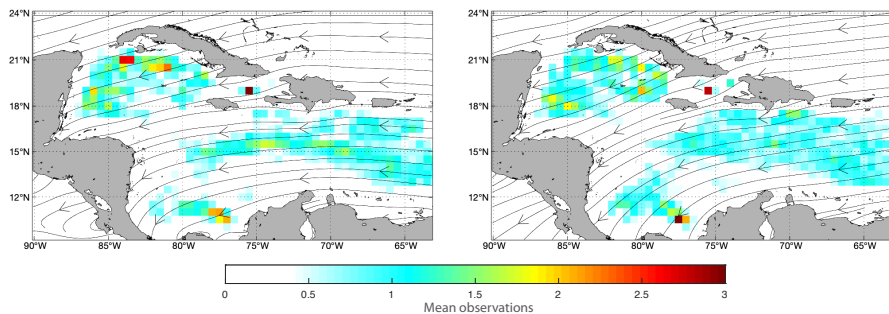


**Fig. 6** Left: streamlines of 10 m height above sea level mean wind during the wet season (December-March), and average number of eddy-observations detected for the same period. Right: the same as in the left but for the dry season (August-November). Wind product is the Cross-Calibrated Multi-Platform (CCMP) Version 2.0, which provides 6-hourly maps at a spatial resolution of  $0.25^\circ \times 0.25^\circ$ . Data is available from 1988 and freely downloadable at <http://www.remss.com/measurements/ccmp/>.

It is worth to note that the highest density of eddy-observations at the lee of the lesser Antilles is found at the left side of the network (Fig. 9), and that they mostly represent the situation given in December-March (Fig. 10) which is the result of the interaction between the inflow of subtropical Atlantic waters of the NBC and the latitudinal wind displacement, which shifts slightly towards the southwest at the eastern boundary.

### 4.3 Monthly and seasonal variability of eddy-observations

From the monthly distribution of eddy-observations (summed in  $0.5 \times 0.5^\circ$  bins), we perform a temporal analysis with the Kohonen Self-Organizing Maps (SOM). SOM is an unsupervised learning neural network especially suited to extract patterns from large data-sets by means of a reduction of the high-dimensional feature space of the input data to a lower-dimensional network of units called neurons (Liu and Weisberg, 2005; Hernández-Carrasco et al, 2018). By applying the SOM in the temporal domain, we can extract zones of covariability (i.e., those regions with a very similar temporal behavior). Each neuron is represented by a weighted vector with a number of components equal to the dimension of the input sample data. In each iteration the neuron whose weighted vector is more similar to the presented input sample data vector is updated together with its topological neighbors. At the end of the training process, the probability density function of the input data is approximated by the SOM, and each unit is associated with a reference pattern that has a number of components equal to the number of variables in the dataset.

First, we compute the SOMs of the monthly eddy observations in the temporal domain with a map size of  $3 \times 2$  (6 neurons or patterns) and a hexagonal

507 map lattice. Fig. 7, shows the six zones of eddy co-variability in the Caribbean  
 508 Sea (to be compared with Fig. 5, left) and Fig. 8 the temporal evolution of  
 509 each of these zones.

510

511

512

513

514

515

516

517

518

519

520

521

522

523

524

525

526

527

528

529

530

531

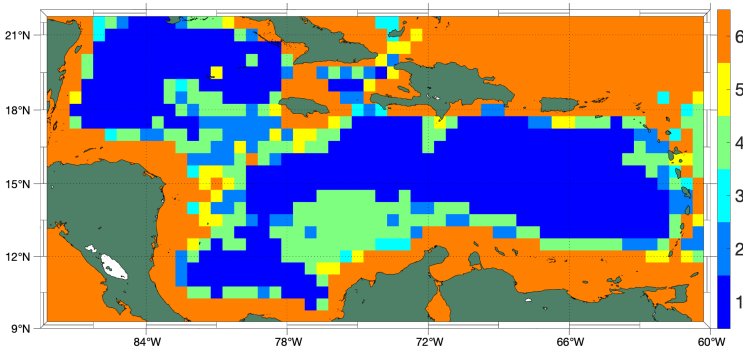


**Fig. 7** Zones of covariability in a  $3 \times 2$  SOM lattice for the monthly distribution of eddy-observations between 1993 and 2019 (both included).

532 The largest area (77% of the total coverage) corresponds to pattern P#6  
 533 (orange color) where eddy-observations are roughly detected (Fig. 9). This  
 534 area covers the northeastern side of the domain (within the Atlantic basin) and  
 535 Caribbean Sea shelf areas, far from the main currents and their instabilities  
 536 induced by the latitudinal ITCZ migration, and also near the coast where  
 537 SLA presents the largest uncertainties. The second largest percentage (13% of  
 538 coverage) is given by P#1 which, as already pointed out, follows the spatial  
 539 distribution of MEKE. The monthly number of eddy-observations in this area  
 540 is on average 0.7 (Fig. 8, top right panel). The averaged monthly detected  
 541 eddy-observations (box inside Fig. 7) does not display large differences in the  
 542 detected observations throughout the year. The rest of the patterns (from P#2  
 543 to P#5) cover between 5.5% and 1% of the area, with mean monthly detected  
 544 eddy-observations ranging between 0.1 (P#3) and 0.3 (P#4).

545 Next, the monthly distribution of eddy-observations is analyzed together  
 546 with the MEKE derived from SSH-based geostrophic velocities. We follow the  
 547 same procedure explained above, but in this case we are interested in obtaining  
 548 the spatial distribution of both fields (Hernández-Carrasco and Orfila, 2018).  
 549 Hence, we are going to apply the SOM in the spatial domain (Fig. 9 shows the 6  
 550 neurons for the monthly eddy-observations distribution and their correspond-  
 551 ing MEKE). The probability of occurrence of the each pattern is included at  
 552 the top right of the upper six panels. The most repeated patterns are P#3

and P#4. The former shows a similar MEKE distribution with the only major difference observed at the CCC, which extends towards the Colombian coast. Although small differences are apparent in P#3, eddies are more southerly distributed occupying the whole central American shore, thus being advected westwards. Looking at the MEKE associated to P#3 and P#4, they clearly represent the wet season (P#3) and the dry season (P#4), respectively, when wind stress is larger at the southern basin inducing high values of MEKE thus rising on average the number of eddies in this area during this season.

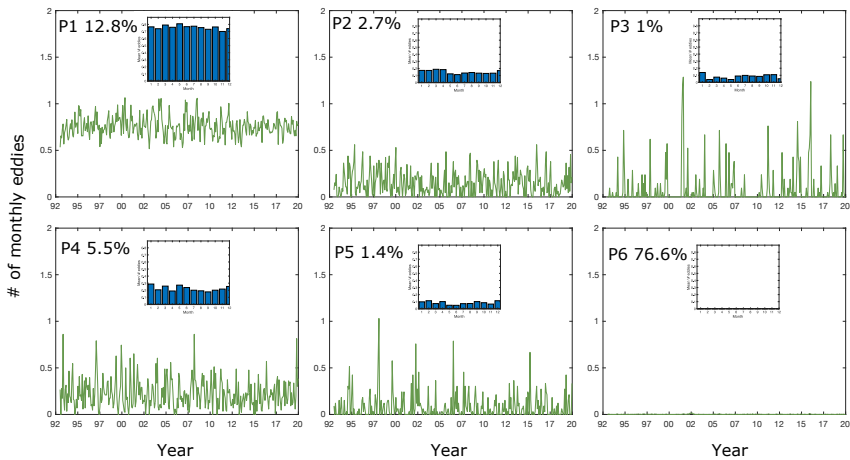


**Fig. 8** Temporal evolution of eddy-observations patterns detected inside each of the 6 areas shown in Fig. 7. The probability of occurrence of each pattern is indicated within each panel. Inner figures correspond to the monthly distribution of eddy-observations associated to each amplitude.

To further study the temporal distribution of patterns we have computed the monthly probability of occurrence of spatial patterns from the BMUs (Fig. 10). The wet season is mainly represented by P#3, while P#4 dominates during the dry season, being in the latter when eddies can reach the southern side of the basin, thus transporting water from the central basin towards the more coastal Caribbean areas.

During the windy season, strong southwestwards winds with their maximum located in the center of the basin produce a strong cross-shore Ekman transport towards the north-northwest, thus contributing to increase MEKE in central Caribbean Sea regions. During these windy months, eddy-observations are mainly distributed over the CC, with a larger distribution over the northern basin. By contrast, during mild wind periods (e.g., October), the most representative pattern is P#2, in which both the CC and the CCC are well developed (see Fig. 9 and Fig. 10), as discussed in Orfila et al (2021).

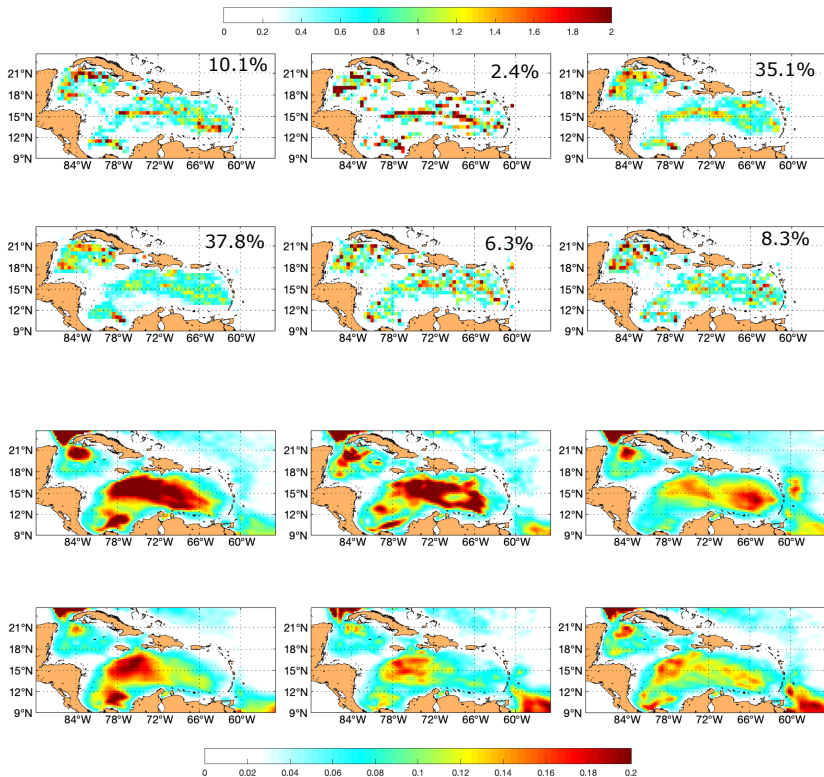


**Fig. 9** SOM neurons in a  $3 \times 2$  lattice for the monthly distribution of eddy-observations (top panels), and their associated  $(\text{MEKE})^{1/2}$  patterns (bottom panels). Units in m/s.

## 5 Conclusions

The work here presented has described the main statistical characteristics as well as the seasonal variability of mesoscale eddies derived from SLA in the Caribbean Sea between 1993 and 2019 (both included). A better understanding of the variability of eddies and their spatial distribution contributes to gain new knowledge on their mechanisms of formation, intensification and dissipation, which have strong implications on biogeochemical and air-sea exchange processes. Since the Caribbean Sea is a semi-enclosed basin, a large part of the advection of nutrients and heat, both in the vertical and in the horizontal, are due to a large extent to eddies.

The spatial distribution of mesoscale eddies reported in this work is consistent with findings from previous observational and model-based studies in which most of the eddies were found to be formed in the eastern Caribbean Sea, or alternatively, had already formed in the northeast of Brazil, although we have also detected a significant number of eddies born in the Yucatan basin.

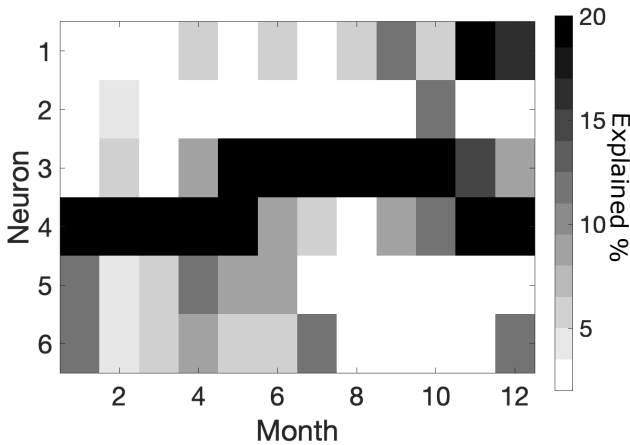


**Fig. 10** Monthly distribution of the patterns provided in Fig. 9.

Some of them stay some time off the Colombian and Venezuelan coasts, while the remainder tend to redistribute around the Cayman and Yucatan basins (Carton and Chao, 1999; Andrade and Barton, 2000; Oey and Lee, 2003; Jouanno et al, 2008; Richardson, 2005; Jouanno et al, 2009; Chelton et al, 2011).

Although many works (Carton and Chao, 1999; Oey and Lee, 2003; Richardson, 2005; Jouanno et al, 2008; van der Boog et al, 2019) have presented a preference for anticyclonic polarity in the Caribbean sea, in this work we find a larger number of CE (54 %) than ACE (46%). There are not significant differences in their respective origin, propagation, amplitude, radius or nonlinearity, although on average CE tend to be more nonlinear than ACE, while ACE are slightly larger. The latter result is in agreement with Jouanno et al (2008), who found that the largest eddies in the Caribbean Sea are anticyclones. The mean lifetime of detected eddies is about two months, although they oscillate between a few weeks and about 10 months. Most eddies travel westwards, although there are a few of them that move eastwards. ACE are thought to be intensified by freshwater river plumes and upwelling events, as they increase the density gradient between the coast and the interior, thus reinforcing the thermal wind balance as they move to the west where the background density and the velocity shear are larger (van der Boog et al, 2019). Most eddies (> 85%) have a lifetime shorter than 120 days. Comparing the results from Carton and Chao (1999) and Oey and Lee (2003), who found the period of spin-up, growth, and drift is approximately 100 days, and with those from Andrade and Barton (2000), who found that the typical timescale of synoptic eddies traveling through the Caribbean Sea is between 100–130 days, it can be concluded that there are no differences between polarities and that there is a general agreement with their longevity.

691 The mean radius detected,  $99.5 \pm 31.2$  km for CE (Fig. 3, h) and  $108.0 \pm 32.4$   
692 km for AE (Fig. 3, i) does not agree with the one provided by [Jouanno et al](#)  
693 (2008), although our results are consistent with the latitudinal distribution  
694 of eddy sizes described by [Chelton et al \(2011\)](#), in which eddies of around  
695 100 km of radius are found in the near-equatorial regions to monotonically  
696 decrease up to 80 km at  $20^\circ$  of latitude. On the other hand, the mean value  
697 of the amplitude ( $7.4 \pm 4.2$  cm for CE and  $6.7 \pm 3.7.2$  cm for AE, see Fig. 3, e  
698 and f, respectively), is consistent with [Gaubé \(2013\)](#), who found that the eddy  
699 field in the Caribbean Sea is characterized by mesoscale eddies with average  
700 amplitudes of 7.8 cm. Besides, we found that eddies are strongly nonlinear,  
701 especially CE, with mean close to 4.

702 Eddies mostly dissipate near the coast of Nicaragua or the Yucatan penin-  
703 sula, and only a few of them are able to travel northwards crossing the Yucatan  
704 basin as already noted by [Carton and Chao \(1999\)](#) and [Chelton et al \(2011\)](#),  
705 who pointed out that eddy disappearance is more frequent near the western  
706 boundaries. However, eddy dissipation in the open ocean can occur by fric-  
707 tional decay or coalescence with other eddies as a consequence of the up-scale  
708 energy cascade of geostrophic turbulence. Some of these terminations may also  
709 occur from temporary or permanent loss of an eddy by the tracking procedure  
710 because of noise in the SLA field or imperfections of the tracking algorithm  
711 ([Chelton et al, 2011](#)). In this regard, [Amores et al \(2018\)](#) also noted that the  
712 number of detected eddies can be significantly underestimated due to the inter-  
713 polation and filtering methods behind the construction of gridded SLA fields,  
714 which can be removing some real SLA eddy-like anomalies. Besides, the trans-  
715 fer of vorticity from the atmosphere to the ocean and the seasonal variability  
716 in the atmospheric forcing may play an important role in the dissipation of  
717 eddies in the basin. Only few eddies are able to pass through the Chibcha  
718 Channel towards the Cayman Sea. Eddies which originated in the southwest-  
719 ern Caribbean Basin are the only ones not advected by the Caribbean Current  
720 nor affected by its instabilities. These eddies tend to remain in the south-  
721 western Caribbean Sea where they form distinctive SLA patterns. [Richardson](#)  
722 (2005) pointed out that many anticyclonic eddies travel westwards up to the  
723 Jamaica Ridge when they are disrupted by topographic-induced dissipation.

724 A seasonal classification of the spatial distribution of eddy-observations  
725 through a neural network based on Self Organized Maps (SOM) showed that  
726 the most representative patterns differ when the analysis is performed by  
727 seasons. Hence the most representative patterns for the different seasons are  
728 P#3, for the dry season and P#4 for the wet season. In both cases eddy-  
729 observations tend to accumulate in the interior of the basin and off the western  
730 Colombian basin, where probably eddies tend to stay longer time due to a par-  
731 tial topographic constrain. However, the complex spatial distribution of eddies  
732 has a periodicity that needs to be further analyzed in future research.

733 To conclude, an open question beyond this research is to analyze how these  
734 mesoscale processes are linked to large scale climate variability, such as El  
735 Niño-Southern Oscillation (e.g., [Sayol et al, 2022](#)), or other signals like the  
736



North Atlantic Oscillation or the Pacific Decadal Oscillation, among other. We leave this task for future work.

## Appendix A Monthly mean surface wind over the Caribbean Sea

Cross-Calibrated Multi Platform (CCMP) near-surface horizontal quasi-global wind fields ( $u, v$ ) -at 10 m over the sea level- have been used in its version 2.0. Winds are provided since 1987 with a spatial resolution of  $0.25^\circ \times 0.25^\circ$  every 6 hours and covers almost all Earth (except poles). This product is the result of an optimal merging of different radiometers, scatterometers, buoys and model data using a variational analysis method.

The monthly mean wind is shown in Fig. A1. Wind streamlines depict the westward direction of the Caribbean low level jet. The maximum intensity is presented during February and July, while the minimum occurs during May and October. For a more detailed explanation on the Caribbean Low level jet and its role on the circulation and dynamics of the region the reader is referred to [Orfila et al \(2021\)](#) and articles therein.

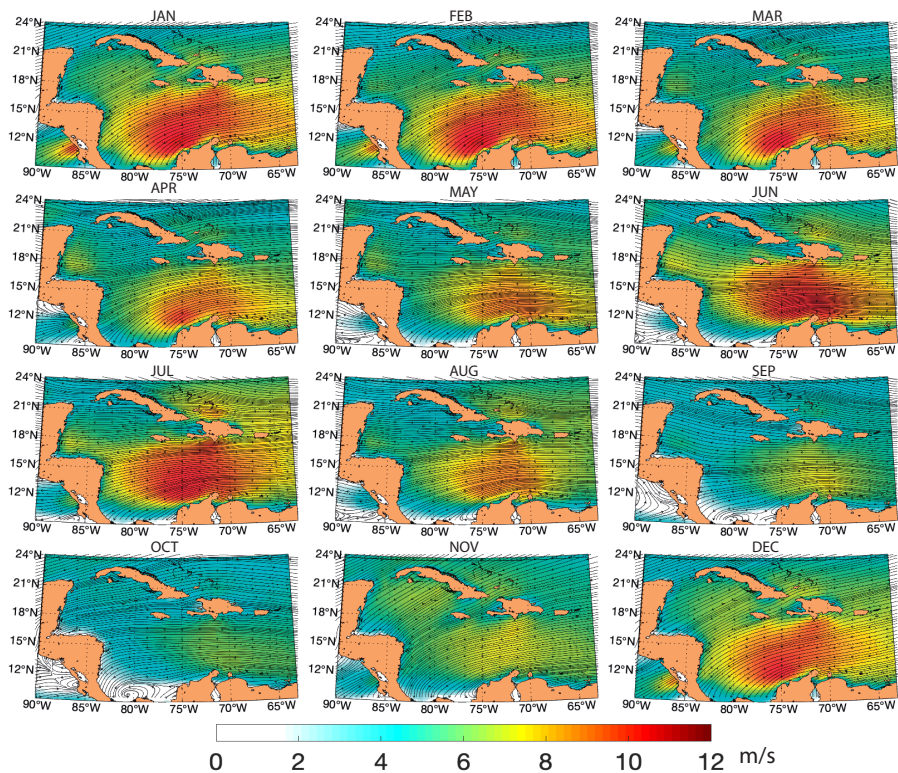


**Fig. A1** Monthly wind intensity and streamlines in the Caribbean sea.

## 783 Appendix B Eddy identification

784 In the following lines the process followed to identify eddies contained in the  
785 eddy atlas (AVISO, 2020) is described in more detail:  
786

787 (i) For each time, there is a two-dimensional value of SSH,  $h(i, j)$ , with four  
788 neighbours. For anticyclonic eddies -concave downward SSH- the identification  
789 is made by defining a pixel  $(i_{ext}, j_{ext})$  as a local positive extreme if the SSH  
790 values of its four neighbors are less than or equal to  $h(i_{ext}, j_{ext})$ . Likewise, for  
791 cyclonic eddies -concave upward SSH-, a pixel  $(i_{ext}, j_{ext})$  is defined to be a  
792 local negative extreme if the SSH values of its four neighbors are greater than  
793 or equal to  $h(i_{ext}, j_{ext})$ .

794 (ii) If we assume an anticyclonic eddy with a local maximum SSH at grid  
795 location  $(i_{ext}, j_{ext})$  and an indicated threshold SSH value  $h_t \leq h(i_{ext}, j_{ext})$ , it  
796 is possible to define  $E(i_{ext}, j_{ext}, h_t)$  as the connected set of pixels  $(i_l, j_l)$ ,  
797  $l = 1, \dots, n$ , which contains  $(i_{ext}, j_{ext})$  and satisfies  $h(i_l, j_l) \geq h_t$ ,  $l = 1, \dots, n$ .  
798 Later, some criteria is applied to seek  $h_b$ , the minimum value of  
799 incrementally decreasing thresholds  $h_t$ , such that the compact and coherent  
800 structure  $E(i_{ext}, j_{ext}, h_b)$ , which is an eddy realization with basic SSH value  
801 of  $h_b$ , satisfies:

802 (a)  $n \leq n_{max}$ , a determined number of pixels in this structure.

803  $n \geq 2$ , a minimum of two interior pixels.

804 (b) Not a single pixel in this structure could have as a neighbor a pixel that  
805 belongs to another eddy.

806 (c) The structure is connected. There are not holes on the edges or within the  
807 interior of the area.

808 (d) Let  $d(i_k, j_k, i_l, j_l)$  be the distance between pixels  $(i_k, j_k)$  and  $(i_l, j_l)$ . So,  
809 the maximum value of  $d(i_k, j_k, i_l, j_l)$  over all pairs of edge pixels in the structure  
810  $E(i_{ext}, j_{ext}, h_t)$  must be less than a specified value  $d_{max}$ .

811 (iii) The set of edge pixels in  $E(i_{ext}, j_{ext}, h_b)$  defines the outer perimeter of  
812 the eddy realization.

813 (iv) Eddies are identified by growing sets of pixels from the single pixels at  
814 the local maximum in  $h(i, j)$  and  $-h(i, j)$  for anticyclonic and cyclonic eddies,  
815 respectively. Hence, given a set of pixels  $E_l$ , the next set  $E_{l+1}$  is computed by  
816 finding all of the neighbors of the edge pixels in  $E_l$  that exceed  $h_{l+1}$ , which are  
817 then added to  $E_l$ . At each step  $E_l$ , all the criteria above described are checked.  
818 If at least one of them is missing, the sequence is stopped. The single pixels at  
819 the local maximum are ordered into decreasing size and eddy recognition are  
820 obtained from successively smaller initial values of  $h$  or  $-h$  without attention  
821 to polarity.

822 After the eddy identification, an approximate calculation of different eddy  
823 characteristics is computed using the following parameters:

- 824 1. The eddy centroid coordinates -longitude and latitude  $(x_c, y_c)$ .
- 825 2. The amplitude A defined as the difference between the extreme SSH value  
826 of  $h(i_{ext}, j_{ext})$  and the average of SSH over the edge pixels that define the  
827 external perimeter of the eddy.  
828

3. The effective radius scale  $L_{eff}$ , which is defined to be the radius of a circle with area equal to that of the set of connected pixels  $E(i_{ext}, j_{ext}, h_b)$ . 829  
830
4. The average of geostrophic speed covering the edge pixels of  $E_l$  is found at each threshold  $h_l \geq h_n$ . The maximum of this average is the rotational or axial speed  $U$  of the eddy where,  $h_U$  is defined as the threshold SSH at which this maximum average occurs. The speed core of the eddy is then the subset of connected pixels  $E(i_{ext}, j_{ext}, h_U)$ . 831  
832  
833  
834  
835
5. The speed-based radius scale  $L$ , which is defined to be the radius of a circle which area is equal to that enclosed by the contour of maximum circum-average geostrophic speed. 836  
837  
838

This algorithm is applied on a  $1/4^\circ \times 1/4^\circ$  grid using a threshold increment of  $\delta = 0.25$  cm and a maximum area  $n_{max} = 2000$  pixels. The distance  $d$  between the two remotest points must be less than  $d_{max} = 400$  km for latitudes greater than  $\pm 25^\circ$  and  $d_{max} = 700$  km lower than  $\pm 25^\circ$  of latitude at the equator, plus an additional restriction of eddies amplitude  $A \geq 1$  cm (Schlax and Chelton, 2016). 839  
840  
841  
842  
843  
844  
845  
846  
847  
848  
849  
850  
851  
852  
853  
854  
855  
856  
857  
858  
859  
860  
861  
862  
863  
864  
865  
866  
867  
868  
869  
870  
871  
872  
873  
874

## 875 **Declarations**

876 **Acknowledgments** Authors would like to thank coffee and the Goldbergh  
877 variations. Also José Luis Perales is greatly acknowledged.  
878

879 **Ethics Approval** Not applicable.

880 **Consent to Participate** Not applicable.

881 **Consent to Publish** Not applicable.

882 **Authors Contributions** M.E.López-ALzate (MELA) developed the statisti-  
883 cals, J.M.Sayol (JMS) the seasonal analysis and A.Orfila (AO) performed the  
884 spatio temporal variability. AO and JMS produced and analyzed the results  
885 with the support of MELA. All authors contributed to read, edit and approve  
886 the final manuscript.  
887

888 **Funding** JMS thanks the joint funding received from the Generalitat Valen-  
889 ciana and the European Social Fund under Grant APOSTD/2020/254. AO  
890 acknowledges financial support from FEDER/Ministerio de Ciencia, Inno-  
891 vación y Universidades – Agencia Estatal de Investigación through MOCCA  
892 project (grant # RTI2018-093941-B-C31), Fundación Iberostar and Univer-  
893 sité de Toulon-VAR. MELA is funded by Corporación CE-Marin through  
894 Convocatoria 14, 2018 supporting PhD candidates.  
895

896 **Competing interests** The authors declare that they have no known com-  
897 peting financial interests or personal relationships that could have appeared  
898 to influence the work reported in this paper. AO is member of the editorial  
899 board of Ocean Dynamics, Ocean Science and Frontiers in Marine Science.  
900

901 **Availability of data and materials** All codes are available from the  
902 corresponding author upon request. Mesoscale eddy atlas is available from  
903 AVISO at [https://www.aviso.altimetry.fr/en/data/products/value-](https://www.aviso.altimetry.fr/en/data/products/value-added-products/global-mesoscale-eddy-trajectory-product.html)  
904 [added-products/global-mesoscale-eddy-trajectory-product.html](https://www.aviso.altimetry.fr/en/data/products/value-added-products/global-mesoscale-eddy-trajectory-product.html) (last  
905 access 25/02/022). Geostrophic velocities provided by CMEMS are available  
906 at <https://climate.copernicus.eu> (last access 25/02/022). Winds are available  
907 from RMSS at <http://www.remss.com/measurements/ccmp/> (last access  
908 25/02/2022).  
909

910  
911  
912  
913  
914  
915  
916  
917  
918  
919  
920

**References**

- Amores A, Jorda G, Arsouze T, et al (2018) Up to what extent can we characterize ocean eddies using present-day gridded altimetric products? *Journal of Geophysical Research: Oceans* 123(10):7220–7236. <https://doi.org/https://doi.org/10.1029/2018JC014140>
- Andrade CA (2000) The circulation and variability of the colombian basin in the caribbean sea. PhD thesis, University of Wales
- Andrade CA, Barton ED (2000) Eddy development and motion in the caribbean sea. *Journal of Geophysics Research* 105(C11):26,191–26,201. <https://doi.org/https://doi.org/10.1029/2000JC000300>
- Andrade CA, Barton ED (2005) The guajira upwelling system. *Continental Shelf Research* 25(9):1003 – 1022. <https://doi.org/10.1016/j.csr.2004.12.012>
- AVISO (2020) Mesoscale Eddy Trajectory Atlas Product Handbook
- Baums IB, Paris CB, Chérubin LM (2006) A bio-oceanographic filter to larval dispersal in a reef-building coral. *Limnology and Oceanography* 51(5):1969–1981. <https://doi.org/10.4319/lo.2006.51.5.1969>
- van der Boog CG, Pietrzak JD, Dijkstra HA, et al (2019) The impact of upwelling on the intensification of anticyclonic ocean eddies in the caribbean sea. *Ocean Science* 15(6):1419–1437. <https://doi.org/10.5194/os-15-1419-2019>
- Bracco A, Pedlosky J, Pickart RS (2008) Eddy Formation near the West Coast of Greenland. *Journal of Physical Oceanography* 38(9):1992–2002. <https://doi.org/10.1175/2008JPO3669.1>
- Capet X, McWilliams JC, Molemaker MJ, et al (2008) Mesoscale to Submesoscale Transition in the California Current System. Part I: Flow Structure, Eddy Flux, and Observational Tests. *Journal of Physical Oceanography* 38(1):29–43. <https://doi.org/10.1175/2007JPO3671.1>
- Carton JA, Chao Y (1999) Caribbean sea eddies inferred from topex/poseidon altimetry and a 1/6° atlantic ocean model simulation. *Journal of Geophysical Research* 104. <https://doi.org/https://doi.org/10.1029/1998JC900081>
- Chang YLK, Miyazawa Y, Béguer-Pon M, et al (2018) Physical and biological roles of mesoscale eddies in japanese eel larvae dispersal in the western north pacific ocean. *Scientific reports* 8(1):5013–5013. <https://doi.org/10.1038/s41598-018-23392-5>

- 967 Chelton DB, deSzoeke RA, Schlax MG, et al (1998) Geographical variability  
968 of the first baroclinic rossby radius of deformation. *Journal of Physical*  
969 *Oceanography* 28(3):433 – 460. [https://doi.org/10.1175/1520-0485\(1998\)0](https://doi.org/10.1175/1520-0485(1998)028(0433:GVOTFB)2.0.CO;2)  
970 [28\(0433:GVOTFB\)2.0.CO;2](https://doi.org/10.1175/1520-0485(1998)028(0433:GVOTFB)2.0.CO;2)  
971
- 972 Chelton DB, Schlax MG, Samelson RM (2011) Global observations of nonlinear  
973 mesoscale eddies. *Progress in Oceanography* 91(2):167 – 216. [https://doi.org](https://doi.org/10.1016/j.pocean.2011.01.002)  
974 [/10.1016/j.pocean.2011.01.002](https://doi.org/10.1016/j.pocean.2011.01.002)  
975
- 976 Chérubin LM, Richardson P (2007) Caribbean current variability and the influ-  
977 ence of the amazon and orinoco freshwater plumes. *Deep Sea Research Part*  
978 *I: Oceanographic Research Papers* 54:1451–1473. [https://doi.org/10.1016/](https://doi.org/10.1016/j.dsr.2007.04.021)  
979 [j.dsr.2007.04.021](https://doi.org/10.1016/j.dsr.2007.04.021)  
980
- 981 Conti D, Orfila A, Mason E, et al (2016) An eddy tracking algorithm based  
982 on dynamical systems theory. *Ocean Dynamics* 66(11):1415–1427. [https:](https://doi.org/10.1007/s10236-016-0990-7)  
983 [//doi.org/10.1007/s10236-016-0990-7](https://doi.org/10.1007/s10236-016-0990-7)  
984
- 985 Farneti R, Delworth TL, Rosati AJ, et al (2010) The Role of Mesoscale Eddies  
986 in the Rectification of the Southern Ocean Response to Climate Change.  
987 *Journal of Physical Oceanography* 40(7):1539–1557. [https://doi.org/10.117](https://doi.org/10.1175/2010JPO4353.1)  
988 [5/2010JPO4353.1](https://doi.org/10.1175/2010JPO4353.1)  
989
- 990 Fratantoni DM, Richardson PL (2006) The Evolution and Demise of North  
991 Brazil Current Rings\*. *Journal of Physical Oceanography* 36(7):1241–1264.  
992 <https://doi.org/10.1175/JPO2907.1>  
993
- 994 Gaube P (2013) Satellite observations of the influence of mesoscale ocean  
995 eddies on near-surface temperature, phytoplankton and surface stress. PhD  
996 thesis, Oregon State University  
997
- 998 Gaube P, Chelton D, Samelson RM, et al (2015) Satellite observations of  
999 mesoscale eddy-induced ekman pumping. *Journal of Physical Oceanography*  
1000 45(45,1):104–132. [https://doi.org/https://doi.org/10.1175/JPO-D-14-003](https://doi.org/https://doi.org/10.1175/JPO-D-14-0032.1)  
1001 [2.1](https://doi.org/https://doi.org/10.1175/JPO-D-14-0032.1)  
1002
- 1003 Goni GJ, Johns WE (2003) Synoptic study of warm rings in the north brazil  
1004 current retroflection region using satellite altimetry. In: Goni G, Malanotte-  
1005 Rizzoli P (eds) *Interhemispheric Water Exchange in the Atlantic Ocean*,  
1006 Elsevier Oceanography Series, vol 68. Elsevier, p 335 – 356, [https://doi.org](https://doi.org/10.1016/S0422-9894(03)80153-8)  
1007 [/10.1016/S0422-9894\(03\)80153-8](https://doi.org/10.1016/S0422-9894(03)80153-8)  
1008
- 1009 Hernández-Carrasco I, Solabarrieta L, Rubio A, et al (2018) Impact of hf radar  
1010 current gap-filling methodologies on the lagrangian assessment of coastal  
1011 dynamics. *Ocean Science* 14(4):827–847. [https://doi.org/10.5194/os-14-82](https://doi.org/10.5194/os-14-827-2018)  
1012 [7-2018](https://doi.org/10.5194/os-14-827-2018)

- Hernández-Carrasco I, Orfila A (2018) The role of an intense front on the connectivity of the western mediterranean sea: The cartagena-tenes front. *Journal of Geophysical Research: Oceans* 123(6):4398–4422. <https://doi.org/10.1029/2017JC013613>
- Ji J, Dong C, Zhang B, et al (2018) Oceanic eddy characteristics and generation mechanisms in the kuroshio extension region. *Journal of Geophysical Research: Oceans* 123(11):8548–8567. <https://doi.org/10.1029/2018JC014196>
- Jochumsen K, Rhein M, Böning SHCW (2010) On the propagation and decay of north brazil current rings. *Journal of Geophysical Research* 115. <https://doi.org/10.1029/2009jc006042>
- Johns WE, Townsend TL, Fratantoni DM, et al (2002) On the atlantic inflow to the caribbean sea. *Deep Sea Research I* 49:211–243. [https://doi.org/10.1016/S0967-0637\(01\)00041-3](https://doi.org/10.1016/S0967-0637(01)00041-3)
- de Jong MF, Bower AS, Furey HH (2016) Seasonal and Interannual Variations of Irminger Ring Formation and Boundary–Interior Heat Exchange in FLAME. *Journal of Physical Oceanography* 46(6):1717–1734. <https://doi.org/10.1175/JPO-D-15-0124.1>
- Jouanno J, Sheinbaum J, Barnier B, et al (2008) The mesoscale variability in the caribbean sea. part i: Simulations and characteristics with an embedded model. *Ocean Modelling* 23:82–101. <https://doi.org/10.1016/j.ocemod.2008.04.002>
- Jouanno J, Sheinbaum J, Barnier B, et al (2009) The mesoscale variability in the caribbean sea. part ii: Energy sources. *Ocean Modelling* 26:226–239. <https://doi.org/10.1016/j.ocemod.2008.10.006>
- Jury MR (2011) Long-term variability and trends in the caribbean sea. *International Journal of Oceanography* 2011. <https://doi.org/10.1155/2011/465810>
- Karstensen J, Schütte F, Pietri A, et al (2017) Upwelling and isolation in oxygen-depleted anticyclonic modewater eddies and implications for nitrate cycling. *Biogeosciences* 14(8):2167–2181. <https://doi.org/10.5194/bg-14-2167-2017>
- Liu Y, Weisberg RH (2005) Patterns of ocean current variability on the west florida shelf using the self-organizing map. *Journal of Geophysical Research: Oceans* 110(C6). <https://doi.org/10.1029/2004JC002786>
- Mason E, Pascual A, McWilliams JC (2014) A New Sea Surface Height–Based Code for Oceanic Mesoscale Eddy Tracking. *Journal of Atmospheric and*

- 1059 Oceanic Technology 31(5):1181–1188. [https://doi.org/10.1175/JTECH-D-](https://doi.org/10.1175/JTECH-D-14-00019.1)  
1060 [14-00019.1](https://doi.org/10.1175/JTECH-D-14-00019.1)
- 1061
- 1062 Molinari R, Spillane M, Brooks I, et al (1981) Surface current in the caribbean  
1063 sea as deduced from lagrangian observations. Journal of Geophysical  
1064 Research 86. <https://doi.org/https://doi.org/10.1029/JC086iC07p06537>
- 1065
- 1066 Oey LY, Lee HC (2003) Effects of winds and caribbean eddies on the fre-  
1067 quency of loop current eddy shedding: A numerical model study. Journal of  
1068 Geophysics Research 108. <https://doi.org/10.1029/2002JC001698>
- 1069
- 1070 Orejarena-Rondón AF, Sayol JM, Marcos M, et al (2019) Coastal impacts  
1071 driven by sea-level rise in cartagena de indias. Frontiers in Marine Science  
1072 6. <https://doi.org/10.3389/fmars.2019.00614>
- 1073
- 1074 Orejarena-Rondón AF, Restrepo JC, Correa-Metrio A, et al (2022) Wave  
1075 energy flux in the caribbean sea: Trends and variability. Renewable Energy  
1076 181:616–629. <https://doi.org/https://doi.org/10.1016/j.renene.2021.09.081>
- 1077
- 1078 Orfila A, Urbano-Latorre CP, Sayol JM, et al (2021) On the impact of the  
1079 caribbean counter current in the guajira upwelling system. Frontiers in  
1080 Marine Science 8. <https://doi.org/10.3389/fmars.2021.626823>
- 1081
- 1082 Pauluhn A, Chao Y (1999) Tracking eddies in the subtropical north-western  
1083 atlantic ocean. Physics and Chemistry of the Earth, Part A: Solid Earth  
1084 and Geodesy 24(4):415 – 421. [https://doi.org/https://doi.org/10.1016/S1](https://doi.org/https://doi.org/10.1016/S1464-1895(99)00052-6)  
1085 [464-1895\(99\)00052-6](https://doi.org/10.1016/S1464-1895(99)00052-6)
- 1086
- 1086 Rennie SJ, Pattiaratchi CP, McCauley RD (2007) Eddy formation through the  
1087 interaction between the leeuwin current, leeuwin undercurrent and topogra-  
1088 phy. Deep Sea Research Part II: Topical Studies in Oceanography 54(8):818  
1089 – 836. <https://doi.org/10.1016/j.dsr2.2007.02.005>, the Leeuwin Current and  
1090 its Eddies
- 1091
- 1092 Richardson PL (2005) Caribbean current and eddies as observed by surface  
1093 drifters. Deep-Sea Research II 52:429–463. [https://doi.org/https://doi.org/](https://doi.org/https://doi.org/10.1016/j.dsr2.2004.11.001)  
1094 [10.1016/j.dsr2.2004.11.001](https://doi.org/10.1016/j.dsr2.2004.11.001)
- 1095
- 1096 Sayol JM, Vásquez LM, Valencia JL, et al (2022) Extension and application  
1097 of an observation-based local climate index aimed to anticipate the impact  
1098 of el niño–southern oscillation events on colombia. International Journal of  
1099 Climatology n/a(n/a). <https://doi.org/https://doi.org/10.1002/joc.7540>
- 1100
- 1101 Schlax MG, Chelton DB (2016) The “growing method” of eddy identification  
1102 and tracking in two and three dimensions. College of Earth, Ocean and  
1103 Atmospheric Sciences Oregon State University, Corvallis, Oregon
- 1104



- Schneider T, Bischoff T, Haug GH (2014) Migrations and dynamics of the intertropical convergence zone. *Nature* 513(7516):45–53. <https://doi.org/10.1038/nature13636>, URL <https://doi.org/10.1038/nature13636>
- Soutelino R, Gangopadhyay A, da Silveira I (2013) The roles of vertical shear and topography on the eddy formation near the site of origin of the brazil current. *Continental Shelf Research* 70:46 – 60. <https://doi.org/10.1016/j.csr.2013.10.001>, oceanography, ecology and management of Abrolhos Bank
- 1105  
1106  
1107  
1108  
1109  
1110  
1111  
1112  
1113  
1114  
1115  
1116  
1117  
1118  
1119  
1120  
1121  
1122  
1123  
1124  
1125  
1126  
1127  
1128  
1129  
1130  
1131  
1132  
1133  
1134  
1135  
1136  
1137  
1138  
1139  
1140  
1141  
1142  
1143  
1144  
1145  
1146  
1147  
1148  
1149  
1150